








Aberration calibration and correction with nano-scatterers in digital holographic microscopy for semiconductor metrology

CHRISTOS MESSINIS,^{1,2,*}  THEODORUS T. M. VAN SCHAIJK,^{1,2} 
NITESH PANDEY,³ ARMAND KOOLEN,³ ILAN SHLESINGER,⁴ 
XIAOMENG LIU,^{1,2} STEFAN WITTE,^{1,2}  JOHANNES F. DE BOER,¹ 
AND ARIE DEN BOEF^{1,2,3}

¹Department of Physics and Astronomy, and LaserLaB, Vrije Universiteit, De Boelelaan 1081, 1081 HV Amsterdam, The Netherlands

²Advanced Research Center for Nanolithography (ARCNL), Science Park 106, 1098 XG Amsterdam, The Netherlands

³ASML Netherlands B.V., De Run 6501, 5504 DR, Veldhoven, The Netherlands

⁴Center for Nanophotonics, AMOLF, Science Park 104, 1098 XG Amsterdam, The Netherlands

*c.messinis@arcnl.nl

Abstract: Overlay metrology measures pattern placement between two layers in a semiconductor chip. The continuous shrinking of device dimensions drives the need to explore novel optical overlay metrology concepts that can address many of the existing metrology challenges. We present a compact dark-field digital holographic microscope that uses only a single imaging lens. Our microscope offers several features that are beneficial for overlay metrology, like a large wavelength range. However, imaging with a single lens results in highly aberrated images. In this work, we present an aberration calibration and correction method using nano-sized point scatterers on a silicon substrate. Computational imaging techniques are used to recover the full wavefront error, and we use this to correct for the lens aberrations. We present measured data to verify the calibration method and we discuss potential calibration error sources that must be considered. A comparison with a ZEMAX calculation is also presented to evaluate the performance of the presented method.

© 2021 Optical Society of America under the terms of the [OSA Open Access Publishing Agreement](#)

1. Introduction

The aggressive reduction of semiconductor device dimensions as stated by Moore's law [1] has driven many improvements in optical wafer metrology and semiconductor processing equipment like lithography. Integrated circuits consist of multilayer complex structures with feature sizes below 10 nm that need to be controlled in terms of placement (overlay, OV) and minimum feature size (Critical Dimension, CD). As a result, overlay and CD need to be robustly measured with sub-nm precision at high throughput on many points on a wafer, requiring small measurement times in the milli-second range [2].

Optical overlay metrology has seen notable advances over the years to keep up with the demanding requirements of the semiconductor industry. For many years image-based overlay metrology (IBO) using box-in-box (BiB) metrology targets has been the main approach. IBO uses a bright-field microscope to create an image of this BiB target and OV is determined by measuring the position of the inner box edges with respect to the outer box edges. Significant improvement of metrology precision and robustness came when the box structures were replaced by gratings. These advanced imaging metrology targets have a smaller size allowing more features in a device and more edges which improves the precision [3,4].

Another big step forward was the introduction of (micro) diffraction-based overlay metrology (DBO) where an overlay target consists of overlapping grating-pairs [5]. DBO is a scatterometry-based technique for measuring overlay on advanced layers at high throughput [6]. DBO measures on metrology targets that consist of small overlapping gratings with approximately $10 \times 10 \mu\text{m}^2$ size. An overlay error between these overlapping gratings creates a small intensity difference between the $+1^{\text{st}}$ and -1^{st} diffraction order, which scales linearly with overlay. Dark-field microscopy with high-quality optics is used to create $+1^{\text{st}}$ and -1^{st} order images of the metrology targets on a camera and these images are used to determine overlay (OV). Robustness and sub-nm accuracy is possible by optimizing the grating etch and using carefully selected multiple wavelengths [7]. However, the relentless push to follow Moore's law drives existing optical overlay metrology to the extreme limits of its possibilities. For example, novel devices and process flows result in the use of new materials that are only sufficiently transparent at infrared wavelengths which drives the need for OV metrology tools that cover a larger wavelength range. In addition, there is a strong push to reduce the size of the metrology targets which requires improved imaging resolution in OV metrology. On top of this, the diffraction efficiency of overlay targets continues to decrease to the 0.01 % levels due to thin resist that is used in EUV lithography and increased light losses in the stack of layers that cover the bottom grating. Last but not least, a solution for all these challenges needs to be realized at acceptable cost and in a small footprint since available space for metrology is limited.

We are exploring dark-field digital holographic microscopy (df-DHM), as a DBO metrology technique that can potentially address these challenges [8]. Our df-DHM uses a supercontinuum source in combination with an acousto-optical tunable filter (AOTF) as a tunable light source and a single uncoated aspheric imaging lens which allows imaging over a large wavelength range since there are no anti-reflecting coatings that limit the usable wavelength range. Moreover, this results in a compact sensor with a high transmission and at acceptable cost. As an alternative for a single imaging lens, a catadioptric Schwarzschild objective could be of interest as well [9]. However, the central obscuration of these objectives limits the freedom in optimizing the wavelength and pitch of a metrology grating for best accuracy and robustness. This makes these objectives less preferred for the high-end metrology applications for which our df-DHM is intended.

However, a single aspheric lens only offers diffraction-limited imaging performance for the wavelength for which the lens was designed. For other wavelengths large aberrations will significantly degrade the image quality to levels that are unacceptable for metrology applications. For example, Fig. 1(b) shows a dark-field image of a grating with a pitch of 400 nm that was obtained with our single-lens setup using a wavelength of 532 nm and an illumination angle of incidence of 70° (Fig. 1(a)). For these measurement settings, the -1^{st} diffracted order passes through the edge of the exit pupil where spherical aberration will lead to a serious image degradation. Figure 1(c) shows the wavefront error in the exit pupil of our lens (Thorlabs A240TM) which has been calculated with ZEMAX optical design software using nominal lens design data. The graph shows the Zernike coefficients of this wavefront error where we have used the fringe-indexing convention (Appendix A). It can be clearly seen that a large 4^{th} order spherical aberration (Z_9) is present that explains the poor imaging quality in Fig. 1(b).

Fortunately, Digital Holographic Microscopy (DHM) is able to correct for these lens aberrations since a hologram allows us to retrieve the complex field of the aberrated image. This complex field can then be back-propagated to the exit pupil where we can apply a wavefront error correction. Calibrating wavefront aberrations in DHM has been a subject of research for many years. It has been shown that the wavefront errors introduced by a microscope objective and lenses can be successively removed in DHM [10,11], as well as spherical aberration [12], chromatic aberration [13], astigmatism [14,15], or anamorphism [16,17]. For the wavefront reconstruction in DHM

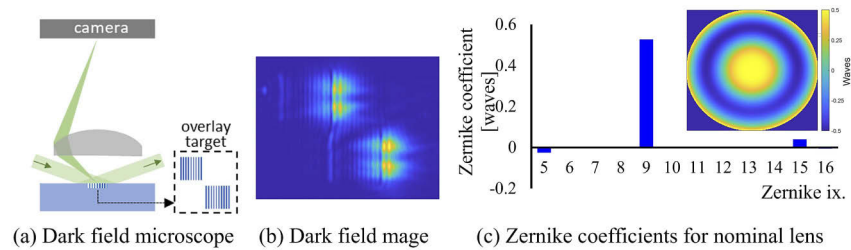


Fig. 1. (a) schematic drawing of a dark field microscope with a 532 nm wavelength and 70° illumination angle. (b) dark field image of 400 nm grating pitch targets. (c) Zernike decomposition for Thorlabs A240TM lens as obtained with ZEMAX for $\lambda = 532$ nm and $NA = 0.465$.

with a single hologram, an accurate knowledge of setup parameters such as the wavefront shape of the reference beam and the object-image distance are critical.

The possibility of correcting lens aberrations in digital holography was first outlined by Stadelmaier and Massig [12]. A pupil-based evaluation of the complex point-spread-function (PSF) was originally proposed by Charrière *et al.* [18], where the complex amplitude point-spread function of a high NA microscope objective was measured with DHM and the retrieved wavefront error was decomposed in a set of Zernike polynomials. In that work the authors used the fiber tip of a scanning near field microscope as a point source.

Here we will present aberration calibration and aberration correction for dark-field DHM by measuring the complex PSF using point scatterers on a flat substrate. In contrast to the work presented in [18,19] we use a single imaging lens with high aberration levels instead of a high-quality microscope objective. Moreover, instead of using a strong point source (a single-mode fiber tip) we use a nanometer-sized scattering structure that has been created on a bare silicon wafer surface. Such a structure can be reproducibly made in various ways and allows an easy and fast in-line aberration calibration in DHM-based wafer metrology. The amount of light that is diffracted from such a small structure is weak, but we will show that the coherent amplification of the reference wave in DHM still allows wavefront calibrations with sub-milli-wave repeatability. We will also show that this method is able to calibrate and correct even very large aberrations in a single lens df-DHM. Finally, our method uses a spherical reference wave coming from the tip of a single-mode fiber without collimation optics. As a result, the reference wavefront shape is known with a high degree of accuracy which helps to reduce wavefront calibration errors.

In the next section we will briefly explain the concept of lens calibration using a point-scatterer in a single-lens DHM setup. We will show that non-telecentric single-lens imaging allows us to use a spherical reference wave coming from the tip of a single mode fiber. We will then present our experimental df-DHM setup followed by a detailed description of the calibration procedure and the measured wavefront aberrations of our single lens. Section 3 presents results of lens aberration calibration with a point source and on the correction that has been applied to highly aberrated images of small grating targets that are used for overlay metrology. Section 4 discusses potential error sources that impact the precision and accuracy of our aberration calibration method and section 5 concludes the paper with an outline of the following steps that we plan to take to improve overlay metrology.

2. Theory

2.1. Imaging model of a single lens digital holographic microscope

Many DHMs create an image of an object with a microscope objective and a tube lens [19,20]. Such a double-telecentric imaging setup introduces no quadratic wavefront curvature in the image and a collimated off-axis reference beam is used to retrieve the complex image via well-known Fourier transform techniques. This collimated reference beam is often made with a beam expander and wavefront errors in this beam expander will impact the retrieved complex image and need to be compensated.

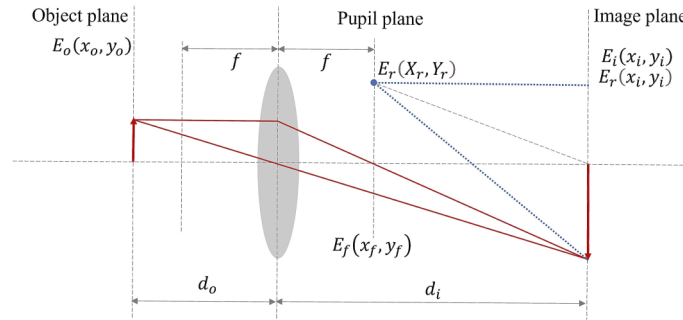


Fig. 2. Schematic drawing of a single lens holographic imaging system, where d_o is the object distance, d_i is the image distance and f is the focal length of the lens. Red solid lines indicate the ray tracing of the object beam while blue dotted lines indicate the presence and orientation of the spherical reference beam.

Alternative designs for DHM use only a microscope objective to produce a magnified image of an object, which is also equivalent to a lensless holographic setup with an object wave emerging directly from the magnified image of the specimen and not from the sample itself [21,22]. Usually, these designs use a lens in the reference beam to produce a spherical reference wave with a curvature that matches the curvature that is created by the microscope objective. The additional optical elements on the reference beam path may add undesired wavefront errors that should also be calibrated.

Our fiber-coupled df-DHM setup, uses a single imaging lens which adds a quadratic wavefront to the complex image field on the camera. At first sight, this quadratic wavefront may seem undesired. However, such a wavefront allows the use of a spherical reference wave which can be created using the tip of a single-mode fiber. This further reduces the required amount of optics and therefore the number of potential error sources.

Using the plane wave propagation model as described by Goodman in [23] we can show that the complex field E_i of the image on the camera is given by:

$$E_i(x_i, y_i) = e^{j \frac{\pi}{\lambda(d_i-f)}(x_i^2 + y_i^2)} \left(H(x_i, y_i) \otimes E_o \left(-\frac{x_i}{M}, -\frac{y_i}{M} \right) \right). \quad (1)$$

Here \otimes denotes a convolution and $H(x_i, y_i)$ is the Fourier transform of the aperture stop in the back focal plane of the lens (for the full derivation of Eq. (1) see Appendix B). H is essentially the complex point-spread-function (PSF) of this single-lens imaging system. $E_o(-\frac{x_i}{M}, -\frac{y_i}{M})$ is the complex field in the object plane and M is the magnification. The quadratic phase term in Eq. (1) has a radius of curvature $d_i - f$ where d_i is the image distance and f is the focal length of the lens. For clarity, the symbols used in Eq. (1) are also indicated in Fig. 2 which shows the paraxial single lens imaging along with the reference beam.

The spherical reference beam E_r at the image plane in our df-DHM has a radius of curvature $d_i - f$ and its complex amplitude in the image plane is given by:

$$E_r(x_i, y_i) = A e^{j \frac{\pi}{\lambda(d_i - f)} ((x_i - X_r)^2 + (y_i - Y_r)^2)}. \quad (2)$$

The reference beam, that is propagated from the tip of a fiber, generates spherical waves that are described with the quadratic phase approximation. The quadratic phase terms in the image field and the reference beam are identical when the fiber tip is positioned in the pupil plane of the imaging lens. In this case the coherent sum of the image field and the reference wave yields an intensity I on the camera:

$$I(x_i, y_i) = |E_i|^2 + A^2 + A e^{j \frac{2\pi}{\lambda(d_i - f)} (x_i X_r + y_i Y_r)} \left(H(x_i, y_i) \otimes E_o \left(-\frac{x_i}{M}, -\frac{y_i}{M} \right) \right) + c.c. \quad (3)$$

In this expression, the term "c.c." denotes the complex conjugate. The quadratic phase terms in the image field and the reference beam are eliminated, and the complex field of the image field can be retrieved with standard Fourier transform techniques.

2.2. Lens calibration and correction with complex point-spread-functions

The usual way to characterize an optical imaging system, is its point-spread function (PSF) which is an image of a single point source. A point source illuminates the lens aperture with a spherical wave that is insensitive to non-uniformity in the illumination beam. Without aberrations, the wavefront in the exit pupil of our df-DHM will be perfectly spherical (Fig. 3), and the point source will be imaged as a diffraction limited Airy disk. However, lens aberrations will deform the wavefront (red curve in Fig. 3) and will result in an aberrated Airy disk with enhanced side lobes and a lower peak intensity. For isoplanatic imaging the PSF is invariant to a shift of the object and in that case a measurement of the complex PSF at 1 point in the field is sufficient to calibrate the aberrations in the imaging system. For this assumption to be valid we keep the object in the center of the field of view (FoV), where any small shifts will not impact the measured wavefront.

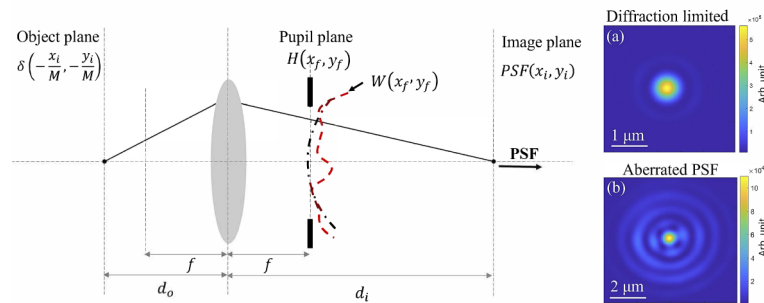


Fig. 3. The lens calibration process with a point source. A point-scatterer illuminates the whole lens aperture. A lens free of aberrations corresponds to a smooth spherical wavefront and a diffraction limited point-spread function (PSF) on the image plane (shown in (a)). A non-ideal lens will deform the wavefront and will result in an aberrated PSF in the image plane (shown in (b)).

For a point source that is centered in the object plane, we find for the retrieved complex PSF in the image plane:

$$PSF(x_i, y_i) = H(x_i, y_i) \otimes \delta \left(-\frac{x_i}{M}, -\frac{y_i}{M} \right). \quad (4)$$

Here, the point source is represented by the Dirac-delta function δ . The complex field can be computationally back-propagated to the pupil plane using a Fourier transform, which yields:

$$\mathcal{F}\{PSF\} = |P(x_f, y_f)| e^{jW(x_f, y_f)}. \quad (5)$$

Here $|P(x_f, y_f)|$ represents the amplitude of the field in the exit pupil and $W(x_f, y_f)$ represents the wavefront aberration of the object wave. In general, this wave aberration is field-dependent. However, non-isoplanatic behavior is usually small for the field sizes that are commonly used in metrology.

Once the lens aberrations have been calibrated with the method as described above, the aberration correction in off-axis DHM is quite straightforward. Fourier transforming the camera image yields the spatial frequency spectrum of the hologram. This consists of a baseband term and two sidebands. These two sidebands are, respectively, the complex field in the exit pupil and its complex conjugate. We select the sideband with the complex field in the exit pupil and we multiply this with the conjugate wavefront error $e^{-jW(x_f, y_f)}$ that we calibrated with the point-scatterer. Then with a second Fourier transform we obtain an aberration-corrected amplitude image of the object.

In practice, the object (a metrology target in our case) is often imaged at a different focus position as the focus position that was used for the aberration calibration. As a result, a (small) focus correction may be needed as well which is easily realized by adding a focus correction term to the field in the exit pupil. The lens aberration and focus correction is given by:

$$\mathcal{F}\{E_{f_{cor}}(x_f, y_f)\} = \mathcal{F}\{E_f(x_f, y_f)\} e^{-jW(x_f, y_f)} e^{-j\alpha_4 Z_4(x_f, y_f)}, \quad (6)$$

where $E_{f_{cor}}(x_f, y_f)$ is the corrected field in the exit pupil, with $e^{-j\alpha_4 Z_4(x_f, y_f)}$ as the focus correction term. The term α_4 represents the amount of defocus and $Z_4(x_f, y_f)$ is the Zernike polynomial, as presented in [24]. The polynomial expression of Z_4 is given in Table 1 of Appendix A. In the following section, we apply this concept to df-DHM to obtain the complex amplitude point-spread function of our imaging system and correct for the aberration introduced by the lens element on an overlay test target.

3. Experimental results of aberration calibration and correction

3.1. Sample preparation

To test the calibration method that we described in the previous section we created two samples with well-defined point objects. The first sample is a bare silicon substrate on which we deposited gold nanoparticles. The nanoparticle solution (A1C-70-CIT-DIH-1-5, Nanopartz) is specified to contain 75 nm gold cubes with citrate ligands that are dispersed in water. For the preparation we cast a drop of 20 μ L on the silicon and after 30 seconds we rinse with ethanol and dry with N_2 (dinitrogen). The size of the nanoparticles was measured to be approximately 80 nm while the shape was varied, with spherical, nanorods or other nanoparticles also present. Potential nanoclusters were also formed at some parts of the sample but for the calibration we used an isolated gold nanoparticle, like the one that is shown in the scanning electron microscope (SEM) image on Fig. 4. The second sample was also fabricated on bare silicon, but now a nano-hole pattern was milled with a 30 keV focused gallium ion beam (FEI Helios Nanolab 600). The ion beam current was set to 100 pA with a focal spot diameter of 80 nm. The nano-hole array was milled in 500 cycles and with a dwell time of 1 ms.

3.2. Experimental setup

To demonstrate DHM capability for lens aberration calibration we selected as our imaging lens an off-the-shelf plano-aspheric lens (Thorlabs A240TM - SL) with an effective focal length of 8 mm and an NA of 0.5. Because of the extreme level of aberrations on the edges of the used lens, we have selected a digital aperture stop of 0.465. This lens is intended for collimating laser diode light with a wavelength of 780 nm and cover glass between the laser and the lens. The lens material was molded glass type D-LAK 6 with a focus shift of 0.35 mm in the visible range. In our experiment, however, we used a 532 nm wavelength and there was no cover glass present

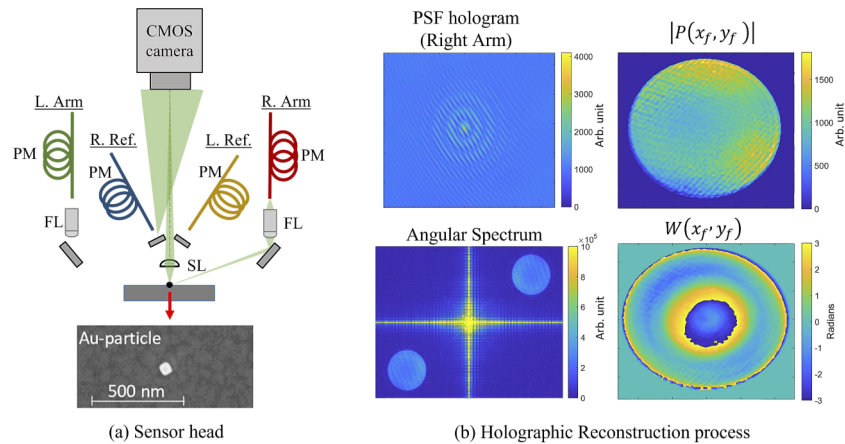


Fig. 4. (a) the fiber-coupled df-DHM. An Au nanoparticle of approximately 80 nm size is illuminated with an oblique illumination beam (R. Arm) of 70° . The object beam will form a PSF that is coherently mixed with the reference beam (R. Ref) resulting in a hologram on image plane. An SEM image of the sample (Au nanoparticle) is shown in the bottom. (b) the holographic reconstruction process. By Fourier transforming the PSF hologram we back-propagate to the pupil plane and the angular spectrum. To retrieve the complex field in the pupil (Eq. (5)), we select one of the sidebands, filter out the other terms and shift it to the origin of the angular spectrum. The right-hand side graphs show the recovered wavefront (amplitude and 2π -wrapped phase of the PSF).

between the object and the lens. As a result, we can expect high spherical aberrations that will result in a severely degraded image of the metrology targets that we are interested in (as already shown in Fig. 1).

The off-axis df-DHM setup (Fig. 4(a)) uses a fiber coupled Supercontinuum White light source (LS; Leukos Rock 400 5) combined with an Acousto-Optical Tunable Filter (AOTF; Gooch & Housego TF550-300-4-6-GH57A). This AOTF device has a bandwidth in the range of 4–7 nm and covers the whole visible wavelength range from 400 to 700 nm. For the majority of the presented experiments, we have selected an AOTF frequency that corresponds to a 532 nm wavelength with a bandwidth of 5 nm. We verified the selected wavelength with a bandpass filter (FLH532-4). A delay line is used to match the optical path of the reference and the illumination beam and polarization maintaining fibers (PM - Shafter-Kirchhoff PMC-400Si-2.3-NA014) are used to couple the light from the source path to the sensor head. The sensor head is comprised of two off-axis illumination arms which illuminate the target from opposite directions at an incident angle of approximately 70° with respect to the normal of the object plane.

For DBO measurements the two sides generate the -1^{st} (L. Arm) and $+1^{\text{st}}$ (R. Arm) diffraction orders. Each illumination arm generates a Gaussian-shaped spot on the object plane ($1/e^2$ diameter approximately $130 \mu\text{m}$) with the use of two microscope objectives (FL- 50X Mitutoyo Plan Apo Infinity Corrected Long WD Objective) and two adjustable mirrors for fine-tuning the angle of incidence. These objectives give a well-defined illumination spot in the whole visible range but at the same time negate the compactness of the setup and increase the total cost. We plan to replace them with small parabolic mirrors that can operate in a broader wavelength range, combined with an illumination beam characterization. In addition, two corresponding spherical reference beams are coherently added to the corresponding object beams. The two reference beams have different azimuthal angles resulting in a different orientation of the sidebands of the spectra of the resulting holograms. With this approach, two holograms are captured by the image sensor using only one image acquisition, and the two object fields can be retrieved with only

three Fast Fourier Transforms (FFTs). Further details of this setup and the parallel acquisition of multiple holograms are given in [8]. The microscope consists of the single plano-aspheric Thorlabs lens (SL) and a camera (Basler acA4112-8gm) with a 12 Mpixel CMOS image sensor with $3.45\ \mu\text{m}$ pixel size. We chose a nominal magnification of 100x by placing our detector 800 mm away from the lens.

3.3. Aberration calibration in dark-field digital holographic microscopy

For calibrating the lens aberration, we used only one of the illumination beams and the corresponding reference beam (R.arm and R.ref in Fig. 4). The illuminated sample contains either gold nanoparticles or nanoholes and light that is scattered from these structures is captured by the lens and creates an aberrated PSF on the camera. This aberrated PSF is coherently mixed with the spherical reference beam and the resulting hologram is used to retrieve the complex PSF. Figure 4(b) shows some of the images in the various steps of the retrieval of the complex PSF and the complex field in the exit pupil.

With df-DHM we obtain the hologram of the PSF and by Fourier transforming we move to the spatial frequency domain (angular spectrum) where the cross-correlation or interference terms of Eq. (3) are fully separated from the baseband. To retrieve the amplitude and the phase of the PSF, using the angular spectrum method that was first outlined by E. Leith and J. Upatnieks [25], we select the sideband that corresponds to the 3rd term of Eq. (3) (top right sideband), filter out the other terms and shift this sideband to the origin of the angular spectrum. This yields the complex field in the exit pupil (Eq. (5)). We could retrieve the PSF in the image plane (Eq. (4)) with an additional FFT, but this is not required for the aberration calibration.

In order to verify our results with ZEMAX, we decompose the wavefront aberrations of the imaging lens into Zernike polynomials [26–28]. ZEMAX simulations generates Zernike coefficients using the fringe-indexing convention [24] which is commonly used by lens designers [29]. More details about Zernike polynomials are summarized in Appendix A.

The wavefront error of the pupil that we recovered with our calibration method, contains 2π phase wrapping errors because of the large spherical aberrations of our lens. This is of no concern for aberration correction as the wrapped phase distribution can be directly used. However in order to quantify the aberrations by a Zernike decomposition, we must apply a 2D phase unwrapping algorithm to the measured wavefront error. The absolute deformation of the phase front can now be decomposed in Zernike polynomials. Figure 5 shows the unwrapped wavefront errors for the two measured samples and a first comparison of the measurements and the ZEMAX prediction in terms of Zernike coefficients.

For this first comparison in Fig. 5 we present the measured wavefront errors of the gold nanoparticle (PSF 1) and the FIB-sample (PSF 2). Using the same color-scale the two wavefronts look almost identical with a small asymmetry on the wavefront error distribution. On the Zernike decomposition of the wavefronts (Fig. 5(a)), it is shown that the two samples are in quite good agreement. Almost all the Zernike coefficients follow the same trend with Z_9 coefficients with only 3 milli-waves difference. The only significant deviation between the two samples is on Z_5 (astigmatism) where we measured a 0.12 waves difference. We are still investigating the main cause for this deviation.

Figure 5(a) also shows the Zernike decomposition of the ZEMAX wavefront. The observed differences between the measured wavefront and the ZEMAX wavefront are due to a combination of lens manufacturing tolerances and residual measurement errors in our setup. The lens in our setup is mass-produced and the tolerance data of this lens are not available but are expected to be significant. In our setup we have also identified a few small error sources that we will discuss in section 4. We also measured the repeatability of the retrieved Zernike coefficients. For each of the two nano-scatterers we acquired 20 holograms under the same conditions and the measured reproducibility of the dominant spherical aberration Z_9 is shown in Fig. 5(b). Despite the small

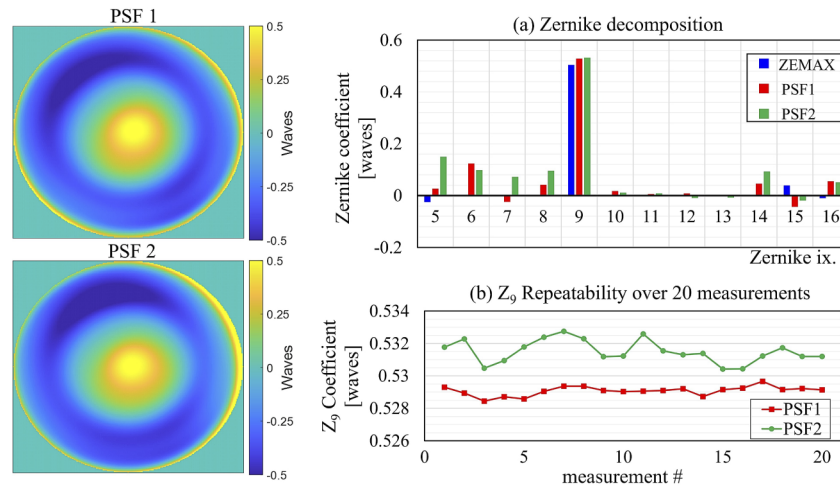


Fig. 5. (a) Zernike decomposition of measured wavefront errors for two different samples along with simulated data as predicted with ZEMAX optical design software (blue bars). PSF 1 (red bars) is the gold nanoparticle and PSF 2 (green bars) is the FIB-sample. The results were obtained for $\lambda = 532$ nm and NA = 0.465. (b) Repeatability measurements of the Z_9 aberration of the measured PSFs.

amount of light scattering, we found a standard deviation of only 0.3 milli-waves for PSF 1 and 0.7 milli-waves for PSF 2.

We also performed a wavefront measurement through focus, and we compared the retrieved Zernike polynomial Z_4 , that correspond to defocus, with the amount of Z_4 that was expected for this lens. Figure 6(a) shows the comparison of the measured data and the expected behavior. These results were obtained by measuring the PSFs for various focus positions. For PSF1 1 μm steps from -6 μm up to +6 μm defocus were obtained along with two more measurements in the extreme cases of ± 10 μm defocus. For PSF2 since the signal for the nanohole array was weaker we limit the measurements to 2 μm steps and align the measured Z_4 with the data for PSF1. As a result, for the second sample the defocus range was from -9 μm up to 5 μm . For larger positive defocus the visibility of the PSF2 was low and we could not complete the measurement. The two sets of measured data change linearly through focus with almost the same slope and with R^2 values of almost unity. There is a small offset in the measured graphs compared to the calculated graphs of approximately 2 μm which can be explained by the fact that the depth-of-focus (DoF) scales with λ/NA^2 which in our case yields a DoF of approximately 2 μm and the best focus position of the measured PSFs was done manually.

Since we ultimately also plan to use our DHM setup over a large wavelength range, we also measured how the amount of spherical aberration Z_9 varies over the wavelength range that we could cover with the AOTF that we currently have in our setup. Figure 6(b) shows the measured through-wavelength Z_9 variation for the gold nanoparticle sample (red dots) and the nanohole sample (green dots), along with the variation predicted by ZEMAX (blue dotted line). It can be seen that our measured wavelength variation is consistent with the behavior that we expect from the dispersive nature of the lens material. Moreover, we also see that our measurement results are in agreement with the ZEMAX calculations. The discrepancy between ZEMAX calculations and measured data can be explained by some uncertainty in the actual wavelength of our AOTF and some uncertainty in the actual NA that was used in the ZEMAX calculation. The AOTF drifts over time and can correspond to an uncertainty on the selected wavelength that deviates from 1-2

nm to 5-10 nm in the whole visible range. At the same time, due to numerical approximations, we estimated an uncertainty of 10^{-3} on the NA that was used in the ZEMAX calculations.

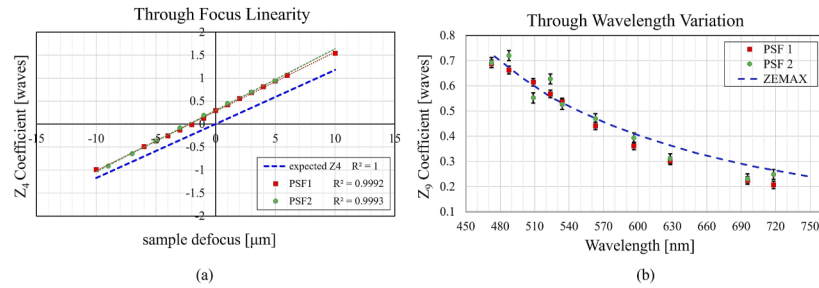


Fig. 6. (a) through focus comparison of the measured PSFs and the predicted slope from ZEMAX. Red squares are the data points of the gold nanoparticle fitted with a red dashed line while the green circles are the data points for the nanohole fitted with a green dotted line. The blue dash-dotted line is the Z_4 slope predicted by a ZEMAX calculation. (b) through wavelength variation of Z_9 of the measured PSFs and the predicted slope from ZEMAX. Red squares are the data points of the gold nanoparticle with error bars indicating an uncertainty of about 15 milli-waves while the green circles are the data points for the nanohole with uncertainty of about 25 milli-waves. The blue dashed line is the Z_9 slope that was calculated with ZEMAX.

In the following subsection we use the calibrated wavefront errors to correct for the lens aberrations and we will show how this improves the imaging of grating targets that are used for OV metrology.

3.4. Aberration correction in dark-field digital holographic microscopy

The df-DHM setup is intended to be used for diffraction-based Overlay metrology on multiple grating targets. To test the aberration correction capabilities of our df-DHM we use a test wafer with overlay targets of small overlapping gratings. The gratings in the bottom layers are etched in a silicon wafer and have an etch depth of about 90 nm. The gratings in the top layer are lithographically made in a resist film with a thickness of about 90 nm. The size of these square gratings varies, and in this experiment, we will focus on gratings of $10 \times 10 \mu\text{m}^2$, $8 \times 8 \mu\text{m}^2$ and $5 \times 5 \mu\text{m}^2$ size and a pitch of 400 nm. This pitch in combination with the used wavelength of 532 nm will result in highly aberrated images since the $\pm 1^{\text{st}}$ diffraction orders are at the edge of the lens aperture where the impact of aberrations is highly visible, as already shown in Fig. 1.

In these measurements we used the left illumination pair (L. Arm) to generate the -1^{st} diffraction order and the right illumination pair (R. Arm) to generate the $+1^{\text{st}}$ diffraction order as shown in Fig. 4. The two holograms were measured in parallel, as explained in [8]. For the calibration the nano-scatterers were also placed at the center of the field of view (FoV). Figure 7 shows the aberration correction process for the image that is formed by the -1^{st} diffraction order.

Figure 7 shows the impact of lens aberrations on the quality of a retrieved image of an overlay target. The highly aberrated image of the targets with a 400 nm grating pitch can significantly affect the overlay measurements since there is not a well-defined target area to measure the total amount of light that is diffracted in the -1^{st} order. Moreover, in real production wafers an overlay target is normally surrounded by patterns and the aberrations would cause a large amount of optical crosstalk from the surrounding patterns into the target area. The correction of the retrieved aberrated image of the -1^{st} diffraction order is shown in Fig. 7. As described in section 2.2, the complex field E_f in the pupil is multiplied by the conjugate wavefront aberration $e^{-jW(x_f, y_f)}$ that we obtained in the calibration step. For the correction of the two diffraction orders the same error

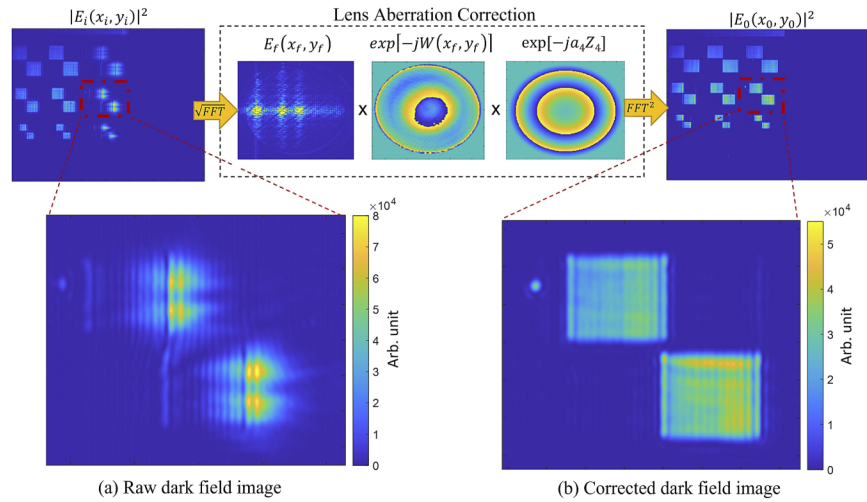


Fig. 7. The aberration correction process for the -1^{st} diffraction order. A retrieved -1^{st} order amplitude of OV targets with df-DHM, $E_i(x_i, y_i)$ is back-propagated to the pupil. In pupil plane we select the cross-correlation term of the -1^{st} order $E_f(x_f, y_f)$ and we filter out the remaining signals. We then multiply the complex field with the phase of the retrieved wavefront error from the calibration $e^{-jW(x_f, y_f)}$ and the focus correction term $e^{-ja_4 Z_4}$. With an additional FFT the corrected image is obtained $E_0(x_i, y_i)$. (a) A close look on the -1^{st} intensity of a highly aberrated target with grating pitch of 400 nm and $8 \times 8 \mu\text{m}^2$ size. (b) a close look of the corrected -1^{st} intensity image of the same target.

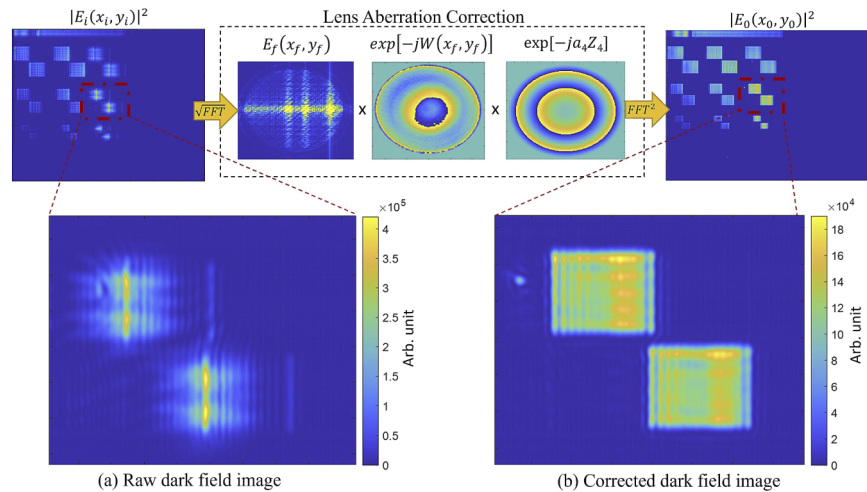


Fig. 8. The aberration correction process for the $+1^{\text{st}}$ diffraction order. A retrieved $+1^{\text{st}}$ order amplitude of OV targets with df-DHM, $E_i(x_i, y_i)$ is back-propagated to the pupil. In pupil plane we select the cross-correlation term of the $+1^{\text{st}}$ order $E_f(x_f, y_f)$ and we filter out the remaining signals. We then multiply the complex field with the phase of the retrieved wavefront error from the calibration $e^{-jW(x_f, y_f)}$ and the focus correction term $e^{-ja_4 Z_4}$. With an additional FFT the corrected image is obtained $E_0(x_i, y_i)$. (a) A close look on the $+1^{\text{st}}$ intensity of a highly aberrated target with grating pitch of 400 nm and $8 \times 8 \mu\text{m}^2$ size. (b) a close look of the corrected $+1^{\text{st}}$ intensity image of the same target.

phase mask was used. Moreover, an additional focus correction $e^{-j\alpha_4 Z_4(x_f, y_f)}$ was also applied since the gold nanoparticle was measured at a (slightly) different focus than the grating sample.

Figure 8 shows the aberration correction of the retrieved df-image for the +1st diffraction order. The correction steps are the same. We are using the same raw hologram from which we reconstruct the raw df-images. For the correction we apply the same wavefront error phase mask and with an additional FFT we obtain the corrected df-image for the +1st diffraction order.

As shown in Fig. 7 and Fig. 8, the -1st and +1st order images of the 400 nm test grating are now nicely corrected resulting in a vast improvement in sharpness. Even an incidental dust particle located on the left of the first grating is now sharply imaged. This significant improvement in image quality will improve metrology performance since the target area is now very localized and well-defined. Moreover, it is expected that crosstalk from surrounding patterns will also be significantly reduced. Before concluding this section, it is important to emphasize that our aberration correction in the exit pupil implicitly assumes that the aberrations are the same for every position in the field. This assumption cannot be generally made. However, for OV metrology we focus on an area of approximately 100 μm^2 and within this region we can assume that the aberrations are the same.

4. Potential error sources in our calibration method

In the previous section we showed that our calibration and correction method significantly improves image quality even in the presence of large aberrations. In this section we will have a closer look at some items that must be considered for the best possible aberration calibration and correction result:

1. size of the selected PSF
2. amplitude inhomogeneity of the reference beam
3. decentering of the virtual field E_f in the exit pupil
4. longitudinal position errors of the reference fiber tip

The first 2 items generally result in very small calibration errors that will impact the quality of aberration correction, so it is imperative to keep them at the milli-wave level. Items 3 and 4 can lead to a significant error in the calibrated wavefront but these errors also occur in the imaging of the metrology target so they will effectively cancel in the aberration correction.

4.1. Size of the selected PSF

The PSF of an aberrated coherent imaging system generally contains many diffraction rings around the central peak. In practice, however, we can only select a finite part of the PSF in a digital hologram. In that case the measured PSF (PSF_{meas}) can be written as the multiplication of the real PSF (PSF_{real}) and a (rotationally symmetric) window function A_W :

$$PSF_{meas}(x_i, y_i) = PSF_{real}(x_i, y_i) * A_W(x_i, y_i). \quad (7)$$

This windowing operation results in a low-pass filtering of the field in the exit pupil since this field will be convolved with the Fourier transform of A_W . This convolution will smoothen steep wavefront variations in the exit pupil so it will result in measured aberrations that are less than the actual aberration. This is clearly visible in Figs. 9(a) and 9(b) which shows the retrieved 4th-order spherical aberration (Z_9) of our lens as function of diameter of the circular window A_W . For the calibration and correction of the overlay targets that we reported in the previous sections we used a circular window with a diameter of 40 μm (indicated with the dashed line in Fig. 9(c)). This window diameter offers a consistency on the measured Z_9 for both samples as many diffraction rings are included and at the same time potential interference from the surroundings is also minimized.

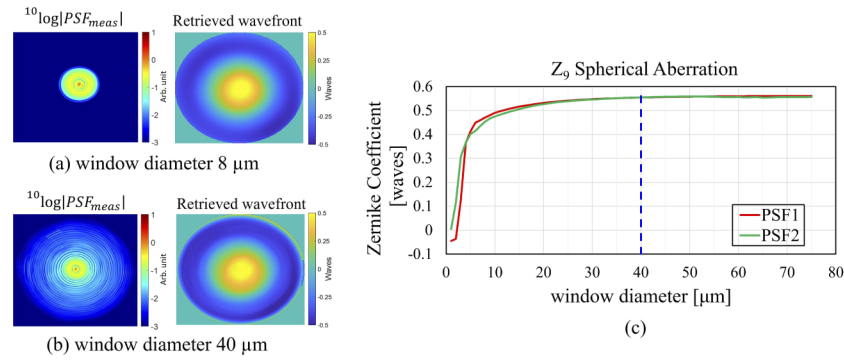


Fig. 9. (a) The retrieved wavefront of a measured PSF that is multiplied by a 8 μm size window. (b) the retrieved wavefront of the same PSF multiplied with a 40 μm window. (c) Measurement variation of Z_9 , spherical aberration of the 2 PSF for different window filtering size that ranges from 1 μm up to 70 μm.

4.2. Amplitude inhomogeneity of the spherical reference beam

In the df-DHM setup (Fig. 4(a)) we use the tip of single mode fiber to generate a well-defined spherical reference wave. To redirect the reference beam to the camera we use a standard half-inch mirror. This additional mirror surface can introduce some micro speckle to the reference beam due to the roughness of the mirror. Moreover, the mirror surface can potentially be degraded over time. The rate of degradation of the coating of the mirror depends on the way the mirror was stored, the humidity and the air flow which can potentially add dust particles in the mirror surface. All these factors can potentially affect the amplitude homogeneity of the reference beam and introduce a small amount of speckle noise in the reference beam.

This speckle noise leads to small amplitude inhomogeneities on the reference beam which affect the retrieval of the complex PSF. This introduces calibration errors on the wavefront measurements, and we need to be sure that the impact on the lens calibration is sufficiently small. To see the impact of the amplitude inhomogeneity we used a first order approximation to correct the hologram from spatial amplitude variations in the reference beam using the following equation:

$$S_{corr} = \frac{S_{DHM} - S_{REF}}{\sqrt{S_{REF}}}. \quad (8)$$

Here S_{DHM} is the acquired digitized camera image of the measured hologram and S_{REF} is the acquired digitized camera image of the measured reference beam. After averaging out the reference beam on a measured hologram we compared the retrieved Zernike coefficients between the raw PSF and the corrected PSF. Figure 10(a) presents the measured intensity of the reference beam where the amplitude inhomogeneities are visible. The inset shows an enhanced contrast image of the speckle noise in a region of interest of about $3.5 \times 1.4 \text{ mm}^2$ at camera level. The relative signal variation in this region was measured to be 2.5% which can be further reduced by using a better-quality mirror. Figure 10(b) presents the Zernike decomposition of the same sample (PSF 1) when the raw measured hologram (Raw PSF) was used compared to the measured hologram after calibrating for the speckle noise of the reference beam using Eq. (8). (Corrected PSF).

As shown in Fig. 10(b), there is a very good correlation between the two wavefronts with Zernike coefficients difference $\Delta_{Zern.Coeff}$ less than 1 milli-wave. This shows that the amplitude inhomogeneity of the reference beam in our experimental setup has a minimum effect on the measured wavefronts and the assumption that we made in section 2.1 is valid.

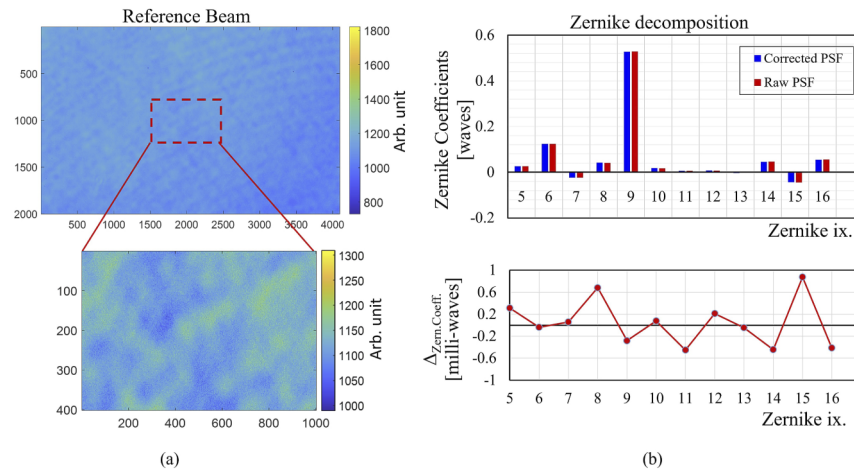


Fig. 10. (a) The measured intensity of the reference beam and a close look on a region of interest with relative speckle noise of 2.5%. (b) the Zernike decomposition of the retrieved wavefronts of the PSF in the two cases along with the difference of the Zernike Coefficients ($\Delta_{Zern.Coeff.}$) of the two wavefronts in milli-waves.

4.3. Decentering of the virtual field E_f in the exit pupil

In the holographic image retrieval, the hologram is initially transformed from the image plane to the pupil plane with a Fourier transform to uncover the baseband signal and the four sideband signals. To retrieve a complex image, we shift the proper sideband term to the origin of the angular spectrum and multiply this with a pupil window (dashed circle in Fig. 11(a)) with a radius that is equal to the NA of the imaging lens. In practice a small offset \vec{s} of the shifted sideband can occur as shown in Fig. 11(a). This will result in a small amount of pupil decentering that lead to small wavefront calibration errors.

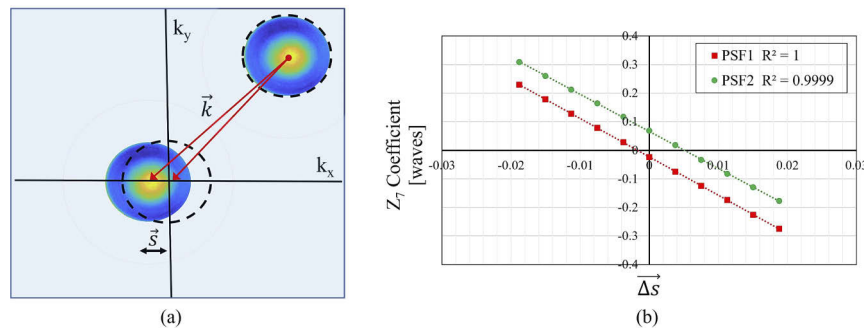


Fig. 11. (a) Schematic drawing of decentering of the exit pupil. (b) Effect of the decentered pupil to coma Z_7 . $\Delta \vec{s}$ is the shift in k space and is equal to λ/FoV .

Figure 11 shows a schematic drawing of the pupil after shifting to the origin of NA space and windowing. In this particular case the window defines the NA stop and blocks all signals outside the sideband. A small error shift \vec{s} will slightly de-center the sideband and introduce wavefront aberrations in a manner that is somewhat similar to additional wavefront aberrations that are introduced by an aperture stop shift as reported in chapter 10 of [27]. For a small shift error and a sufficiently smooth wavefront we can approximate the wavefront of the shifted sideband by a

Taylor expansion:

$$W(\vec{k} + \vec{s}) = W(\vec{k}) + \nabla W \cdot \vec{s}. \quad (9)$$

Here ∇W denotes the gradient of the wavefront W . A large 4th order spherical aberration (Z_9) in combination with a shift \vec{s} (in either k_x or k_y) shows up as, respectively X-coma (Z_7) and Y-coma (Z_8). To show this effect we start with the wavefront error of Z_9 :

$$W_9 = \alpha_9(6\rho^4 - 6\rho^2 + 1). \quad (10)$$

Here α_9 represents the amount of spherical aberration Z_9 which is multiplied with the Zernike polynomial, expressed in waves and $\rho = \sqrt{\rho_x^2 + \rho_y^2}$ is the normalized radial pupil position. A small shift in $\Delta\rho_x$ results in a new wavefront $W_{9,\Delta}$:

$$W_{9,\Delta} = W_9 + \frac{dW_9}{d\rho} \frac{d\rho}{d\rho_x} \Delta\rho_x. \quad (11)$$

Evaluating the 2nd term shows that the shifted wavefront introduces X-coma and a tilt in x-direction:

$$W_{9,\Delta} = W_9 + \Delta\rho_x Z_9(24\rho^3 - 12\rho) \cos \phi. \quad (12)$$

The 3rd order coma is described by the Zernike polynomial $W_7 = \alpha_7(3\rho^3 - 2\rho) \cos \phi$ (see Appendix A). So the small shift $\Delta\rho_x$ introduces a coma increment with a ΔZ_7 given by:

$$\Delta Z_7 = 8\alpha_9 \frac{\Delta k_x}{NA_{obj}}. \quad (13)$$

Here NA_{obj} is the edge of the objective's NA. This analysis shows that a small shift error only becomes significant for lenses with large spherical aberrations that we have in our setup. Fortunately, this shift error also occurs in the imaging of the metrology target so residual wavefront calibration errors will effectively drop out in the aberration correction.

Figure 11(b) shows the effect of small decentering errors. In this numerical experiment we have deliberately introduced a shift in the k_x direction in the range about -0.02 to +0.02 in k-space. It can be clearly seen that the retrieved amount of X-coma varies linearly with the amount of shift.

4.4. Longitudinal position errors of the reference fiber tip

In section 2.1 we presented the single lens DHM where the fiber tip of the reference beam is located in the pupil plane as shown in Fig. 2. In DHM the Z-position of the reference beam defines the Z-location of the Fourier plane where we have the virtual NA stop. However, in practice small longitudinal position errors of the reference fiber tip can occur that result in a mismatch between the Z-location of the virtual Fourier plane and the actual exit pupil of the imaging lens. Here we will show that this results in additional field-dependent coma. The cause of this field-dependent coma is similar to the effect that we described in the previous section and is further clarified in Fig. 12(a). An off-axis position of the point-scatterer will result in a tilted wavefront behind the lens. This tilt in combination with a Z-offset of the virtual aperture will introduce additional coma that scales linearly with field position of the nano-scatterer. On Fig. 12(a) an over-exaggerating drawing is used to highlight the impact of these position errors.

We estimated the longitudinal position error d_{fx} of the reference fiber tip in our setup to be approximately 15 mm, as shown in Fig. 12(a). To evaluate the effect of this position error, we measured the wavefront error as function of x-position of the gold nanoparticle. We determined the X-coma (Z_7) and plotted the measured Z_7 as function of x-position in the field. The result is shown in Fig. 12(b) along with the ZEMAX calculation that was done for an aperture stop that was 15 mm away from the exit pupil. The bottom graph of Fig. 12(b) represents the deviation from a straight line of the measured data.

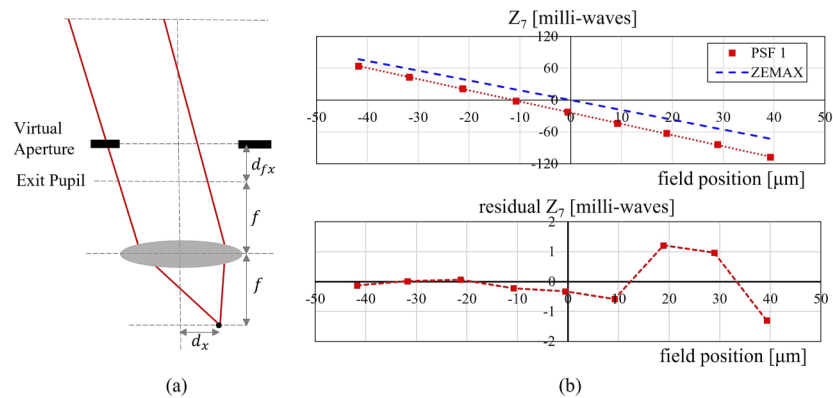


Fig. 12. (a) schematic drawing of the measured distances in the setup, d_x is the field position variation and d_{fx} is the longitudinal error shift of the reference fiber tip. (b)(Top) Through field comparison of the measured PSF and the predicted slope from ZEMAX. Red dots are the data points of the gold nanoparticle fitted with a dashed line while the solid blue line is the expected Z_7 slope by ZEMAX. (Bottom) the deviation of the measured data from the fitted line.

We observe that our measured data is in good agreement with the ZEMAX calculations. The small difference in the slope can be caused by a residual measurement error of the fiber Z-position. The offset of the measured coma may be real or due to a small offset of the virtual aperture as explained in the previous section. The deviation of the measured coma as function of field position from the expected linear behavior is on average below 1 milli-wave which demonstrates the capability of achieving milli-wave calibration precision using weakly scattering nanostructures.

The field-dependent coma that is introduced by a reference fiber Z-misalignment results in non-isoplanatic imaging where aberration cannot be efficiently corrected. It is therefore essential that the fiber tip is placed as closely as possible to the exit pupil. We checked with ZEMAX that this indeed resulted in a negligibly small field-dependent coma for our Thorlabs lens.

5. Conclusion

We have demonstrated a robust method for measuring aberrations and correcting the aberrated images in a df-DHM. We presented measured data that shows that weak point scatterers are very suitable for calibrating large wavefront aberrations in Digital Holographic Microscopy. Although our setup still contained some imperfections like a longitudinal offset of the reference fiber, we have been able to show convincing data of the aberration correction capabilities of our technique. Uncorrected images of metrology targets on a test wafer looked severely distorted but this image quality dramatically improved after applying an aberration correction.

The measured data that we have shown has been measured at only 1 wavelength, but this calibration method is expected to perform well over a wide wavelength range. At longer wavelengths the amount of light that is scattered by a point-scatterer will be significantly reduced. However, since we use an AOTF as a wavelength tuning device the bandwidth of the measurement light will also go up which results in higher intensity levels of the illumination beam. Moreover, the noise in the measured wavefront is in the sub-milli-wave level and is still well below the few milli-wave level that we need.

The wavefront errors measured with a nanohole and a gold nanoparticle were very similar, but we did observe a small ($\approx \lambda/10$) but significant difference in astigmatism (Z_5). One possible cause might be the actual shape of the gold nanoparticle. It provides stronger signals but poor control of

the particle shape. The nanohole sample made with the focused ion beam milling tool combined with scanning electron microscopy (FIB-SEM) on the other hand offers excellent control on the nanohole dimensions but the scattering is weaker. Given the already good reproducibility performance we believe that a FIB-SEM -created nanohole target is the better option for further experiment and we plan to explore this in more detail.

The measurement data in section 4.4 have shown that a longitudinal offset of the reference fiber tip creates a position dependent coma that varies linearly in the field. This will lead to non-isoplanatic imaging conditions that limits the aberration correction capabilities to a small field of view. However, we plan to fix this longitudinal offset and ZEMAX simulations show that this will significantly increase the field size over which we can computationally correct for aberrations.

The results presented here are a stepping-stone towards the next step in this investigation. Now that we can correct aberrations, we can start exploring the overlay metrology capability of our DHM concept in the case when the metrology targets are surrounded by other structures. The broad point-spread-function (PSF) in the presence of aberrations will lead to severe optical crosstalk from the surrounding structures to the metrology target and degrade metrology performance. The excellent aberration correction capabilities that we have demonstrated here are expected to significantly reduce this optical crosstalk error. Demonstrating and quantifying this improvement will be the next step in this investigation.

Appendix A. Zernike coefficients

Zernike polynomials are a mathematical description of a 3D wavefront deviation from a plane wave. Every surface deviation is described by a set of circular symmetrical orthogonal basis functions defined over a unit circle. By this scheme the Zernike Polynomials are defined as:

$$Z_n^{\pm m} = Z_j = R_n^m(\rho) \begin{cases} \cos m\phi & \text{for } +m \\ \sin m\phi & \text{for } -m \end{cases}, \quad (14)$$

where m is a positive or zero integer, and $R_n^m(\rho)$ is the radial factor given by

$$R_n^m(\rho) = \sum_{s=0}^{(n-m)/2} \frac{(-1)^s (n-s)!}{s! (\frac{n+m}{2} - s)! (\frac{n-m}{2} - s)!} \rho^{n-2s}. \quad (15)$$

The norm of a Zernike polynomial is then given by

$$N_{nm} = |Z_n^{\pm m}(\rho, \phi)|^2 = \int_0^{2\pi} \int_0^1 Z_n^{\pm m}(\rho, \phi) Z_n^{\pm m}(\rho, \phi) \rho d\rho d\phi = \frac{\pi(1 + \delta_{0m})}{2(n+1)}. \quad (16)$$

This norm, however, is not used by programs like ZEMAX. The following table, Table 1, provides a list of the first 16 Zernike polynomials to be used in the wavefront aberration function expansion in both standard and Fringe notation. These polynomials are commonly used for wavefront calibration since they are well adapted to accurately describe the phase aberrations in the pupil aberration function.

Table 1. The first 16 Zernike polynomials as a function of (ρ, ϕ) .

Fringe notation	Standard Notation	Zernike Polynomial	Description
$Z_1(\rho, \phi)$	$Z_0^0(\rho, \phi)$	1	piston
$Z_2(\rho, \phi)$	$Z_1^1(\rho, \phi)$	$\rho \cos \phi$	tilt
$Z_3(\rho, \phi)$	$Z_1^{-1}(\rho, \phi)$	$\rho \sin \phi$	tilt
$Z_4(\rho, \phi)$	$Z_2^0(\rho, \phi)$	$2\rho^2 - 1$	focus
$Z_5(\rho, \phi)$	$Z_2^2(\rho, \phi)$	$\rho^2 \cos 2\phi$	astigmatism
$Z_6(\rho, \phi)$	$Z_2^{-2}(\rho, \phi)$	$\rho^2 \sin 2\phi$	astigmatism
$Z_7(\rho, \phi)$	$Z_3^1(\rho, \phi)$	$(3\rho^3 - 2\rho) \cos \phi$	coma
$Z_8(\rho, \phi)$	$Z_3^{-1}(\rho, \phi)$	$(3\rho^3 - 2\rho) \sin \phi$	coma
$Z_9(\rho, \phi)$	$Z_4^0(\rho, \phi)$	$6\rho^4 - 6\rho^2 + 1$	spherical
$Z_{10}(\rho, \phi)$	$Z_3^3(\rho, \phi)$	$\rho^3 \cos 3\phi$	trefoil
$Z_{11}(\rho, \phi)$	$Z_3^{-3}(\rho, \phi)$	$\rho^3 \sin 3\phi$	trefoil
$Z_{12}(\rho, \phi)$	$Z_4^2(\rho, \phi)$	$(4\rho^4 - 3\rho^2) \cos 2\phi$	oblique spherical
$Z_{13}(\rho, \phi)$	$Z_4^{-2}(\rho, \phi)$	$(4\rho^4 - 3\rho^2) \sin 2\phi$	oblique spherical
$Z_{14}(\rho, \phi)$	$Z_5^1(\rho, \phi)$	$(10\rho^5 - 12\rho^3 + 3\rho) \cos \phi$	5 th order coma
$Z_{15}(\rho, \phi)$	$Z_5^{-1}(\rho, \phi)$	$(10\rho^5 - 12\rho^3 + 3\rho) \sin \phi$	5 th order coma
$Z_{16}(\rho, \phi)$	$Z_6^0(\rho, \phi)$	$20\rho^6 - 30\rho^4 + 12\rho^2 - 1$	spherical

Appendix B. Derivation of Eq. (1)

We derive Eq. (1) in a two-step process:

1. we first calculate the field E_f in the back focal plane of the lens
2. we then obtain the field E_i the image plane by propagating the field E_f to the image plane using the Fresnel approximation as outlined in chapter 4 of [23].

According to Eq. (6–25) in [23] the complex field E_f in the back focal plane of the lens is given by:

$$E_f(x_f, y_f) = P(x_f, y_f) \iint_{-\infty}^{\infty} E_o(x_o, y_o) e^{-j\frac{2\pi}{\lambda f}(x_o x_f + y_o y_f)} dx_o dy_o. \quad (17)$$

Where P is a quadratic phase term given by:

$$P(x_f, y_f) = \frac{A(x_f, y_f)}{j\lambda f} e^{-j\frac{\pi}{\lambda f} \left(\frac{d_o}{f} - 1\right) (x_f^2 + y_f^2)}. \quad (18)$$

Here A denotes the aperture stop in the back focal plane. Assuming Fresnel diffraction we can write for the the field E_i at a distance d_i from the lens is:

$$E_i(x_i, y_i) = e^{-j\frac{\pi}{\lambda(d_i-f)}(x_i^2 + y_i^2)} \iint_{-\infty}^{\infty} E_f(x_f, y_f) G(x_f, y_f) e^{-j\frac{2\pi}{\lambda(d_i-f)}(x_f x_i + y_f y_i)} dx_f dy_f. \quad (19)$$

where G is a quadratic phase term given by:

$$G(x_f, y_f) = e^{j\frac{\pi}{\lambda(d_i-f)}(x_f^2 + y_f^2)}. \quad (20)$$

We now use the paraxial imaging condition $1/d_o + 1/d_i = 1/f$ and the magnification $M = d_i/d_o$ and substitute Eq. (17) in Eq. (19). This yields Eq. (1):

$$E_i(x_i, y_i) = e^{j\frac{\pi}{\lambda(d_i-f)}(x_i^2 + y_i^2)} \left(H(x_i, y_i) \otimes E_o \left(-\frac{x_i}{M}, -\frac{y_i}{M} \right) \right). \quad (21)$$

where H is the Fourier transform of the aperture stop A :

$$H_i(x_i, y_i) = \iint_{-\infty}^{\infty} A(x_f, y_f) e^{-j \frac{2\pi}{\lambda(d_i-f)} (x_f x_i + y_f y_i)} dx_f dy_f. \quad (22)$$

Funding. ASML; Advanced Research Center for Nanolithography (ARCNL); Vrije Universiteit Amsterdam.

Acknowledgements. We would like to thank Marco Konijnenburg, Head Software Engineering group of AMOLF/ARCNL, and Bartjan Spaanderman, technician of Computational Imaging group of ARCNL for their support and contribution to this project.

Disclosures. The authors declare no conflicts of interest. The authors declare that they have patents or patent applications. The authors Nitesh Pandey, Armand Koolen and Arie den Boef are employees of ASML.

Data availability. Data underlying the results presented in this paper are not publicly available at this time but may be obtained from the authors upon reasonable request.

References

1. G. E. Moore, "Cramming more components onto integrated circuits, reprinted from electronics, volume 38, number 8, april 19, 1965, pp. 114 ff," *IEEE Solid-State Circuits Soc. Newsl.* **11**(3), 33–35 (2006).
2. A. J. den Boef, "Optical wafer metrology sensors for process-robust cd and overlay control in semiconductor device manufacturing," *Surf. Topogr.: Metrol. Prop.* **4**(2), 023001 (2016).
3. M. Adel, M. Ghinovker, B. Golovanevsky, P. Izikson, E. Kassel, D. Yaffe, A. M. Bruckstein, R. Goldenberg, Y. Rubner, and M. Rudzsky, "Optimized overlay metrology marks: theory and experiment," *IEEE Trans. Semicond. Manufact.* **17**(2), 166–179 (2004).
4. M. Adel, D. Kandel, V. Levinski, J. Seligson, and A. Kuniavsky, "Diffraction order control in overlay metrology: a review of the roadmap options," in *Metrology, Inspection, and Process Control for Microlithography XXII*, vol. 6922 J. A. Allgair and C. J. Raymond, eds., International Society for Optics and Photonics (SPIE, 2008), pp. 23–41.
5. W. Yang, R. Lowe-Webb, S. Rabello, J. Hu, J.-Y. Lin, J. D. Heaton, M. V. Dusa, A. J. den Boef, M. van der Schaar, and A. Hunter, "Novel diffraction-based spectroscopic method for overlay metrology," in *Metrology, Inspection, and Process Control for Microlithography XVII*, vol. 5038 (International Society for Optics and Photonics, 2003), pp. 200–207.
6. K. Bhattacharyya, M. Noot, H. Chang, S. Liao, K. Chang, B. Gosali, E. Su, C. Wang, A. den Boef, C. Fouquet, G.-T. Huang, K.-H. Chen, K. Cheng, and J. Lin, "Multi-wavelength approach towards on-product overlay accuracy and robustness," in *Metrology, Inspection, and Process Control for Microlithography XXXII*, vol. 10585 V. A. Ukraintsev, ed., International Society for Optics and Photonics (SPIE, 2018), pp. 326–333.
7. J. Kim, J. Lee, C. Hwang, S. Y. Lee, W. Jung, J. Park, K. Bhattacharyya, A. den Boef, S. Mathijssen, M. Noot, F. Farhadzadeh, D. Park, K. Padhye, S.-R. Jeon, S.-B. Yang, W.-J. Jang, and O.-S. Kwon, "Taking the multi-wavelength DBO to the next level of accuracy and robustness," in *Metrology, Inspection, and Process Control for Microlithography XXXIV*, vol. 11325 O. Adan and J. C. Robinson, eds., International Society for Optics and Photonics (SPIE, 2020), pp. 222–227.
8. C. Messinis, T. T. M. van Schaijk, N. Pandey, V. T. Tenner, S. Witte, J. F. de Boer, and A. den Boef, "Diffraction-based overlay metrology using angular-multiplexed acquisition of dark-field digital holograms," *Opt. Express* **28**(25), 37419–37435 (2020).
9. D. S. Grey, "A new series of microscope objectives: Ii. preliminary investigation of catadioptric schwarzchild systems*," *J. Opt. Soc. Am.* **39**(9), 723–728 (1949).
10. E. Cuhe, P. Marquet, and C. Depeursinge, "Simultaneous amplitude-contrast and quantitative phase-contrast microscopy by numerical reconstruction of fresnel off-axis holograms," *Appl. Opt.* **38**(34), 6994–7001 (1999).
11. G. Pedrini, S. Schedin, and H. J. Tiziani, "Aberration compensation in digital holographic reconstruction of microscopic objects," *J. Mod. Opt.* **48**(6), 1035–1041 (2001).
12. A. Stadelmaier and J. H. Massig, "Compensation of lens aberrations in digital holography," *Opt. Lett.* **25**(22), 1630–1632 (2000).
13. S. D. Nicola, A. Finizio, G. Pierattini, D. Alfieri, S. Grilli, L. Sansone, and P. Ferraro, "Recovering correct phase information in multiwavelength digital holographic microscopy by compensation for chromatic aberrations," *Opt. Lett.* **30**(20), 2706–2708 (2005).
14. S. D. Nicola, P. Ferraro, A. Finizio, and G. Pierattini, "Wave front reconstruction of fresnel off-axis holograms with compensation of aberrations by means of phase-shifting digital holography," *Opt. Lasers Eng.* **37**(4), 331–340 (2002).
15. S. Grilli, P. Ferraro, S. D. Nicola, A. Finizio, G. Pierattini, and R. Meucci, "Whole optical wavefields reconstruction by digital holography," *Opt. Express* **9**(6), 294–302 (2001).
16. S. D. Nicola, P. Ferraro, A. Finizio, and G. Pierattini, "Correct-image reconstruction in the presence of severe anamorphism by means of digital holography," *Opt. Lett.* **26**(13), 974–976 (2001).
17. S. D. Nicola, A. Finizio, G. Pierattini, P. Ferraro, and D. Alfieri, "Angular spectrum method with correction of anamorphism for numerical reconstruction of digital holograms on tilted planes," *Opt. Express* **13**(24), 9935–9940 (2005).

18. F. Charrière, A. Marian, T. Colom, P. Marquet, and C. Depeursinge, "Amplitude point-spread function measurement of high-na microscope objectives by digital holographic microscopy," *Opt. Lett.* **32**(16), 2456–2458 (2007).
19. T. Colom, *Numerical aberrations compensation and polarization imaging in digital holographic microscopy* (EPFL, Lausanne, 2006), chap. 3, pp. 59–72.
20. M. K. Kim, "Principles and techniques of digital holographic microscopy," *J. Photonics Energy* **1**(1), 018005 (2010).
21. A. Doblas, C. Buitrago-Duque, A. Robinson, and J. Garcia-Sucerquia, "Phase-shifting digital holographic microscopy with an iterative blind reconstruction algorithm," *Appl. Opt.* **58**(34), G311–G317 (2019).
22. T. Colom, J. Kühn, F. Charrière, C. Depeursinge, P. Marquet, and N. Aspert, "Total aberrations compensation in digital holographic microscopy with a reference conjugated hologram," *Opt. Express* **14**(10), 4300–4306 (2006).
23. J. W. Goodman, *Introduction to Fourier optics, 4th ed.* (W.H. Freeman and Co., 2017), chap. 4-6, pp. 75–166.
24. R. W. Gray, C. Dunn, K. P. Thompson, and J. P. Rolland, "An analytic expression for the field dependence of zernike polynomials in rotationally symmetric optical systems," *Opt. Express* **20**(15), 16436–16449 (2012).
25. E. N. Leith and J. Upatnieks, "Reconstructed wavefronts and communication theory," *J. Opt. Soc. Am.* **52**(10), 1123–1130 (1962).
26. J. Ruoff and M. Totzeck, "Orientation Zernike polynomials: a useful way to describe the polarization effects of optical imaging systems," *J. Micro/Nanolithogr., MEMS, MOEMS* **8**(3), 031404 (2009).
27. J. Sasián, *Introduction to Aberrations in Optical Imaging Systems* (Cambridge University, 2012).
28. V. N. Mahajan, *Aberration Theory Made Simple, Second Edition* (SPIE Press, 2011).
29. "Optics and optical instruments – preparation of drawings for optical elements and systems – part 5: Surface form tolerances," ISO 10110-5:1996(E), ICS (1996).